are shown as a dotted line and those predicted using the present method are shown as a solid line. The experimental prediction is shown as a solid square. Again, the present results and those predicted by the Thwaites method are in good agreement till before the point of separation for the same reasons explained before. As seen from the graph, the location of the point of separation is in agreement with the experimental prediction of Bussman and Ulrich. The streamlines for the J025 airfoil are shown in Fig. 3. This case is considered a massive separation case, since the dimension of the bubble is of the same order as the dimension of the body, which is an indication of the generality of the algorithm of handling massive separation problems without any difficulty. The last set of results are shown for NACA-0012 airfoil at $Re = 12{,}500$. An arbitrary C-type grid used for that case is shown in Fig. 8, Ref. 1. The values of $(\bar{C}_f)$ are shown in Fig. 4. From that figure, it is clear that the flow separation at $(X/C) = 0.8178$. Swanson and Turkel used a multistage time-stepping scheme for the Navier-Stokes equations to solve for that airfoil using a C-type grid. Their predictions indicated flow separation at $X/C \simeq 0.817$. On the other hand, Rubin reported flow separation at $X/C \simeq 0.84$ for $Re = 12{,}500$. It should be mentioned that the grid used by Rubin was an H-type grid, which is not highly recommended for viscous flow computation. The streamline contours are given in Fig. 10, Ref. 1. For higher Reynolds number values, the nature of the flow is not steady laminar. To be able to handle solutions for higher Reynolds numbers, the transition from laminar to turbulent must be accounted for in the numerical solution. That work is the subject of a current study.

Concluding Remarks

The following statements provide a summary of the more important conclusions that can be extracted from the preceding text:

1) The governing equations are written in a general coordinate system, so flows past arbitrary airfoils can be solved using the present formulation.

2) Second-order-accurate (in space) conservative differences are generated by considering the integral formulation of the governing equations.

3) The algorithm used a marching procedure for solving the ANS equations in the viscous region, similar to the type of numerical solution used for the boundary-layer equations; thus, it can be classified as a boundary-layer-type scheme. Furthermore, the ANS equations have been efficiently coupling in a fully implicit manner with the inviscid stream function equation.

4) Solutions were obtained for J012, NACA-0012, and J025 airfoils.

5) For the J025 airfoil, the flow separated in agreement with the experimental data of Bussmann and Ulrich.

References

[1]Halim, A.A.M., "A Global Marching Technique for the Prediction of Separated Flows over Arbitrary Airfoils," AIAA Paper 87-0591, 1987.

[2]Halim, A.A.M., "Development of an Iterative Boundary Layer-Type Solver for Axisymmetric Separated Flows," *AIAA Journal*, Vol. 24, Aug. 1986, pp. 1298–1304.

Similarity of Ejector Wall-Pressure Distributions

M.S. Chandrasekhara* and A. Krothapalli†
Florida State University, Tallahassee, Florida
and
D. Baganoff‡
Stanford University, Stanford, California

Introduction

THE mechanics of thrust augmentation, using ejectors, can be explained with the help of the pressure distribution found on the ejector surface. Often, the pressure distribution along the wall is also used to describe the mixing process that occurs inside the ejector duct. For example, the location at which the primary jet meets the ejector shroud can be easily obtained from the wall-pressure distribution. These distributions are generally plotted in terms of a normalized pressure coefficient defined as

$$C_p = \frac{p(x) - p_{amb}}{p_t - p_{amb}}$$

where $p(x)$ and p_t denote the local surface pressure and throat pressure respectively while p_{amb} represents the pressure in the ambient medium (see Fig. 1).

When the primary jet operates near or above the critical pressure ratio (stagnation pressure/ambient pressure), the pressure profiles exhibit different behavior for different operating pressure ratios. This observation was made by Quinn[1] for an axisymmetric ejector and by Hsia[2] for a rectangular jet ejector. The lack of similarity in the profiles was attributed to the different mixing phenomena that occur inside the duct for different pressure ratios, and this has been related[1,2] to the generation of "screech tones," which are commonly observed in free underexpanded jets, and their subsequent interaction with the primary jet.

Interestingly, the pressure distributions plotted in the same coordinates for multiple-jet ejectors show self-similarity for all operating conditions, including underexpanded nozzle-pressure ratios. This is because of the *absence* of strong acoustic interactions, which were observed by Hsia[2] for the case of a single-jet ejector. This Note was prompted by the conspicuous absence of these acoustic interactions in both subsonic and supersonic multiple jets.

Description of the Facility and Experiment

The experiments carried out used the same blowdown facility and model as those described in Ref. 3. The jet assembly consisted of a linear array of rectangular jets of 0.3×5.0-cm exit dimensions mounted on a wedge with a 70-deg included angle (see Fig. 1). The jets were spaced at 2.4 cm apart. The shroud enclosing these jets was rectangular in cross section, and its area could be varied to simulate an ejector with an arbitrary area ratio $\mathcal{A}R$. Typically, $\mathcal{A}R = 20{:}1$, 26:1, and 33:1 were used. Also, the location of the

Received Aug. 19, 1985; revision received March 5, 1987.

*Visiting Assistant Professor, Mechanical Engineering Department, FAMU/FSU College of Engineering. Senior Member AIAA.

†Professor, Mechanical Engineering Department, FAMU/FSU College of Engineering. Senior Member AIAA.

‡Professor, Department of Aeronautics and Astronautics. Member AIAA.

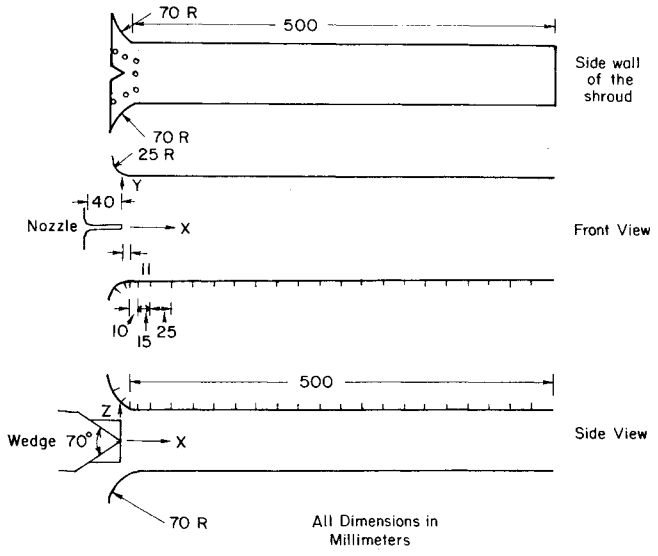

Fig. 1 Schematic of the multiple-jet ejector.

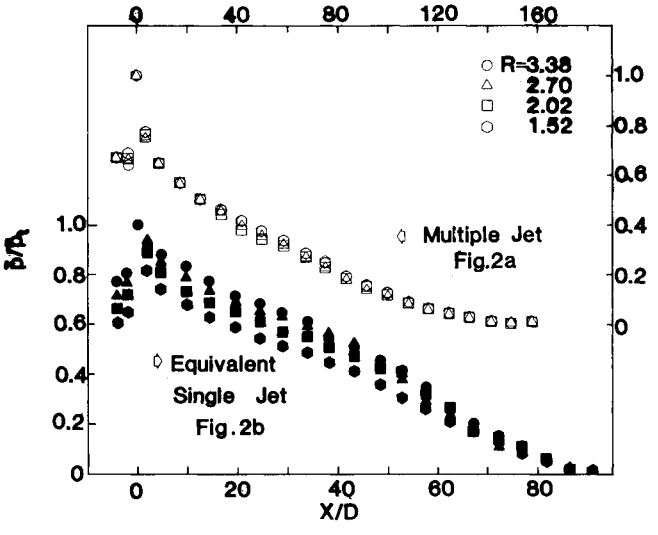

Fig. 2 Wall static pressure distribution for $\mathcal{AR}=20:1$.

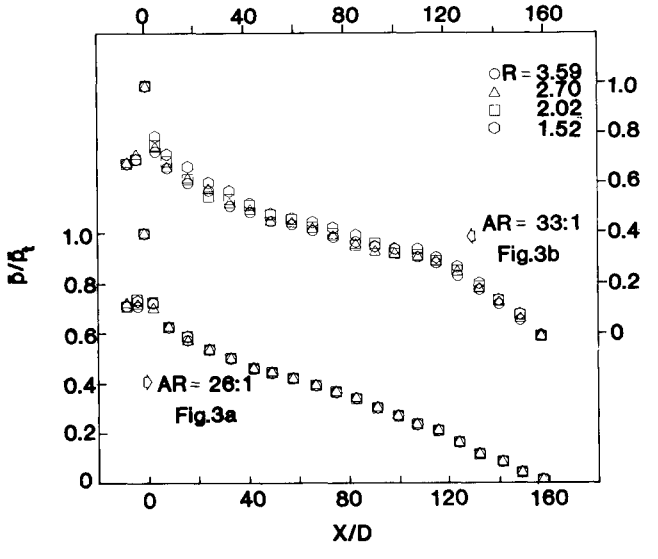

Fig. 3 Wall static pressure distribution in a multiple-jet ejector.

lip and thus the throat of the ejector could be varied by over 10 slot widths relative to the jet exit plane (see Fig. 1).

Static pressure taps were located on all four walls and the inlet bell-mouth of the shroud. These details are shown in Fig. 1. As can be seen from the figure, more locations were chosen on the inlet fairing, as in this region the pressure variation is the most drastic. The pressures reported are the average of the static pressures measured on three walls on any given Y-Z plane. The pressure taps were connected to a four-barrel, 24-port scanivalve that was operated and controlled through a PDP 11/23 computer. The four barrels of the scanivalve were connected to four pressure transducers (± 2.5 psig). In order to account for any transient effects, the transducer output voltage was digitized and averaged over ½ s during scanning. Effectively, 100 samples were collected over a 500-ms duration.

The primary air supply was obtained by charging a reservoir to a high pressure (2400 psig) and draining it via a large settling chamber with screens and a smooth, two-dimensional contraction. All necessary precautions were taken to hold the air-supply pressure variation to less than 0.1 psi. For further details, see Chandrasekhara et al.[3]

Results and Discussion

Figures 2–4 are plotted to show the average of the wall static pressures $\bar{p}$ (on three walls) in the axial plane, normalized by the average throat static pressure $\bar{p}_t$ against the streamwise distance X/D. This particular normalization was chosen because it reveals some very interesting features of the flow, as described in the introduction.

Figure 2a shows the distribution for a three-jet ejector with an area ratio of 20:1 at a nozzle exit plane to ejector shroud throat plane separation distance (NT) of 1.1 cm. These are plotted for nozzle-pressure ratios of $R=1.52$ (corresponding to $M=0.8$), 2.02, 2.70, and 3.38. Self-similarity of the profiles is evident for all of the cases (in both subsonic and supersonic exit conditions). The fact that self-similarity is seen clearly means that screech-tone interactions are absent in the high-speed, multiple-jet ejector. This result was also confirmed by the schlieren pictures for these operating conditions.[3]

Figure 2b presents the normalized pressure distribution for the case of an equivalent single-jet ejector (ESJ). The equivalent single-jet ejector is defined as an ejector with a single primary jet but with the same exit momentum, aspect ratio, and total area as the multiple-jet array studied. It is important to remember that, whereas such a jet does not reproduce the primary and secondary flows in their totality (the nozzle boundary layers, the pressure field between the jets, etc.), it still provides a comparison basis for analyzing and interpreting the multiple-jet results. It is observed from

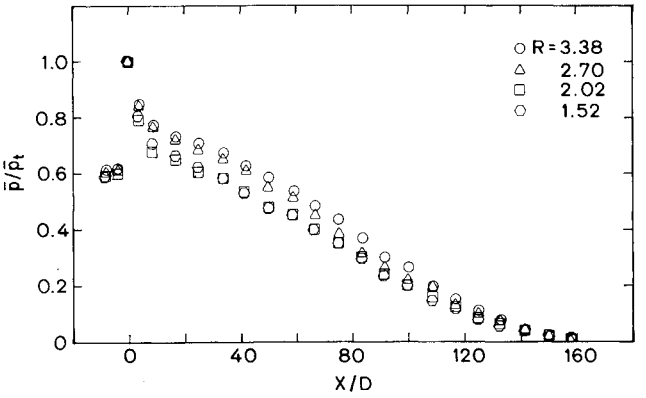

Fig. 4 Wall static pressure distribution in a multiple-jet ejector; $\mathcal{AR}=20:1$, N to T distance = 5.2 cm.

Fig. 2b that the pressure distribution is not self-similar for all pressure ratios. The observed merging of the profiles near the outlet is due to the boundary condition imposed at the duct exit. The lack of self-similarity in the ESJ can be explained by the presence of screech tones and their interactions. The jet behavior changes with the pressure ratio because the mixing characteristics are controlled by these interactions. For a single rectangular-jet ejector, the schlieren pictures of Hsia[2] and those taken in this study show this clearly. However, for the case of the multiple underexpanded jet, no such dominant discrete tones could be found.

Figures 3a and 3b show the self-similarity previously discussed for the case of the multiple-jet ejector for $AR = 26{:}1$ and 33:1. Results similar to those seen in Fig. 2b were obtained for the ESJ ejector at $AR = 26{:}1$ and 33:1, and these are presented and discussed in Chandrasekhara et al.[3]

Furthermore, the self-similarity is present only for short ejector nozzle to throat distances. At a large distance (5.2 cm), a clear breakdown can be seen (Fig. 4), even for $AR = 20{:}1$. This is because the jets tend to behave like freejets near the nozzle exit and generate discrete tones.

Conclusions

The wall static pressure distribution of a multiple underexpanded jet ejector scales well with the average throat static pressure. This is due to the absence of the well-defined acoustic interaction generally observed in the single underexpanded jet. The self-similarity obtained is for short nozzle to throat distances only.

Acknowledgment

This work was supported by the Air Force Office of Scientific Research under Contract F49620-79-0189. The authors appreciate the assistance of Ms. Pam Williams in the preparation of the original manuscript.

References

[1]Quinn, B., "Ejector Performance at High Temperatures and Pressures," *Journal of Aircraft*, Vol. 13, 1976, pp. 948–954.

[2]Hsia, Y.C., "An Experimental Investigation of an Underexpanded Rectangular Jet Ejector," Ph.D. Thesis, Dept. of Aeronautics and Astronautics, Stanford Univ., CA, March 1984.

[3]Chandrasekhara, M.S., Krothapalli, A., and Baganoff, D., "Mixing Characteristics of an Underexpanded Multiple Jet Ejector," JIAA TR-55, Stanford Univ., CA, June 1984.

Buckling of Shear-Deformable Plates

N. R. Senthilnathan,* S. P. Lim,† K. H. Lee,† and S. T. Chow‡
National University of Singapore, Singapore

Introduction

DESPITE the analytic simplicity, Kirchhoff's theory of plates cannot be employed reliably to analyze plates where shear deformation is known to have a significant effect. Reissner[1] was the first to present a shear-deformation theory of plates. Mindlin[2] presented a first-order theory of plates where he accounted for shear deformation in conjunction with a shear-correction factor. The present theory is obtained from Reddy's theory[3] using the assumption that the in-plane rotation tensor through the thickness is constant. The critical buckling loads obtained for isotropic, orthotropic, and composite laminates using the present theory agree very well with the results presented by Reddy and Phan.[4]

Many higher-order theories were also presented which include the effect of shear deformation directly by incorporating the higher-order terms in the displacement functions (for example, see Refs. 5 and 6). A fully three-dimensional theory of plates,[7] and a simple theory for plate bending[8] has also been given. All these theories involve many variables. Reddy[3] recently presented a simple higher-order theory of plates with five variables. This was done by neglecting transverse normal strain and imposing zero transverse shear strains at the two free surfaces using the theory of Lo et al. In the present paper, further simplifying assumptions given by 1) $w = w^b + w^s$, where w is the transverse displacement of the midplane plane and w^b and w^s are its components due to bending and shear, respectively, and 2) $\phi_n = -\nabla w^b$ where ϕ_n is the rotation vector, are made to Reddy's theory so that the number of variables is reduced by one. These assumptions imply that the in-plane rotation tensor is constant through the thickness and will be shown to have little effect on the critical buckling loads obtained for isotropic, orthotropic, and composite laminates. It is interesting to note certain common features between the present theory and the theories by Bhashyam and Gallagher[9] and by KrishnaMurty.[10] Bhashyam and Gallagher used the assumption $w = w^b + w^s$ in conjunction with Mindlin's theory. Thus, they had to introduce a shear correction factor. KrishnaMurty's theory also employed the same assumption but has one variable more than that of Reddy's theory.

Theory

Displacements

The displacement functions by Reddy[3] are given as

$$u = u_0 + z\left[\phi_x - \frac{4z^2}{3h^2}\left(\frac{\partial w}{\partial x} + \phi_x\right)\right]$$

$$v = v_0 + z\left[\phi_y - \frac{4z^2}{3h^2}\left(\frac{\partial w}{\partial y} + \phi_y\right)\right] \qquad w = w_0 \tag{1}$$

where u_0, v_0, and w_0 are the in-plane and transverse displacements at the midplane, ϕ_x and ϕ_y are the rotations of the normals to the cross sections, h and plate thickness, and z the coordinate in the tranverse direction. By making further assumptions given by

$$w_0 = w^b + w^s \qquad \phi_x = -w,_x^b \text{ and } \phi_y = -w,_y^b \tag{2}$$

It is seen that the functions given by Eq. (1) now take the simpler form

$$u = u_0 - z\frac{\partial w^b}{\partial x} - \frac{4z^3}{3h^2}\frac{\partial w^s}{\partial x}$$

$$v = v_0 - z\frac{\partial w^b}{\partial y} - \frac{4z^3}{3h^2}\frac{\partial w^s}{\partial y} \qquad w = w^b + w^s \tag{3}$$

Received June 30, 1986; revision received Jan. 26, 1987.

*Graduate Student, Department of Mechanical and Production Engineering.

†Lecturer, Department of Mechanical and Production Engineering.

‡Professor, Department of Mechanical and Production Engineering.